Jet-Installation Noise Reduction with Permeable Flaps at In-Flight Conditions

Rego, Leandro; Zamponi, R.; Ragni, D.; Avallone, F.; Casalino, D.; Cruellas Bordes, M.

DOI
10.2514/6.2022-2874

Publication date
2022

Document Version
Final published version

Published in
28th AIAA/CEAS Aeroacoustics 2022 Conference

Aeroacoustics Conferences
June 14-17, 2022, Southampton, UK
28th AIAA/CEAS Aeroacoustics 2022 Conference

10.2514/6.2022-2874

Jet-Installation Noise Reduction with Permeable Flaps at In-Flight Conditions

Leandro Rego*, Riccardo Zamponi†, Daniele Ragni‡, Francesco Avallone§, Damiano Casalino¶
Delft University of Technology, Delft, 2629HS, The Netherlands

Marc Cruellas Bordes‖
German-Dutch Wind Tunnels (DNW), Marknesse, 8316 PR, The Netherlands

An experimental investigation on jet-installation noise reduction with permeable flaps on an aircraft half-model is performed, focusing on the effects on the noise levels as well as on the aerodynamic properties of the model (lift and drag forces). A nozzle with an exit diameter D_j = 113 mm is included for generating a single-stream jet flow in the vicinity of the airframe. Two perforated flaps with different hole distributions are investigated. The first one has a uniform hole distribution with equal hole spacing in both streamwise and spanwise directions, whereas the second one has a gradient permeability with the hole spacing progressively decreasing towards the trailing edge. Aerodynamic force measurements, carried out with a balance, show that the permeable flaps are responsible for a lift reduction in the order of 7%, and a slight drag increase, in the order of 0.5%, with the gradient permeability flap outperforming the uniform one. Flow-field maps indicate that the effect on lift is linked to the formation of side-edge vortices at the spanwise positions corresponding to the discontinuity between solid and porous regions. Acoustic results obtained from phased array measurements show that the source at the flap trailing edge, generated by the interaction with the jet, reduces by 3 dB in amplitude with both permeable flaps, which perform similarly. Therefore, the permeable flaps are able to significantly reduce jet-installation noise for an aircraft configuration in flight conditions, however care must be taken in the design of the permeable structure in order to avoid aerodynamic degradation.

I. Introduction

The high bypass ratio of aircraft turbofan engines has led to a significant reduction in fuel burn, as well as in jet noise emissions due to a lower exhaust velocity [1]. However, these engines have large diameters in order to generate the necessary amount of thrust and, due to their size, they have to be mounted closer to the wing to maintain a minimum ground clearance. This increased proximity results in an interaction between the jet flow and nearby airframe surfaces such as the wing and flap, and the generation of a noise source known as Jet-Installation Noise (JIN) [2]. This source is especially significant during take-off and approach flight conditions, when the deployed high-lift systems are positioned close to the jet [3]. Recent computational results of aircraft acoustic footprint have shown that installation effects are responsible for penalties of approximately 4 EPNdB at full aircraft level [4]. In the near future, with the development of ultra-high bypass ratio engines, this source will likely become more dominant due to increased proximity between engine and airframe [5], and thus it is necessary to develop and study feasible noise reduction solutions.

The dominant source for JIN is located at the surface trailing edge, which acts as a discontinuity region for convecting hydrodynamic pressure waves generated in the jet mixing-layer, resulting in their scattering as noise. This phenomenon is responsible for noise increase at low and mid frequencies, particularly in the directions normal and upstream of the jet axis, equivalent to a distribution of acoustic dipoles at the trailing-edge [6–8]. Installation effects are also responsible for reflection of acoustic waves generated by quadrupole sources in the jet plume [9] and acoustic shielding on the opposite side of the surface [10].

*PhD Candidate, Department of Aerodynamics, Wind Energy, Flight Performance and Propulsion, l.rego@tudelft.nl, AIAA Student Member
†Postdoctoral Researcher, Department of Aerodynamics, Wind Energy, Flight Performance and Propulsion, r.zamponi@tudelft.nl, AIAA Member
‡Associate Professor, Department of Aerodynamics, Wind Energy, Flight Performance and Propulsion, d.ragni@tudelft.nl, AIAA Member
§Assistant Professor, Department of Aerodynamics, Wind Energy, Flight Performance and Propulsion, f.avallone@tudelft.nl, AIAA Member
¶Professor, Department of Aerodynamics, Wind Energy, Flight Performance and Propulsion, d.casalino@tudelft.nl, AIAA Member
‖Project Manager, Business Unit LLF/AM; Projects and Customer Relation Management, Marc.CruellasBordes@dnw.aero

A solution for JIN reduction is the application of flow-permeable materials on the scattering surface. Permeable materials have been widely used as noise reduction solutions for several aeroacoustic applications such as airfoil trailing-edge noise [11–14] and turbulence-impingement noise [15–17]. For JIN in a configuration comprised by a flat plate placed in the vicinity of a single-stream jet, measurements by Rego et al. [18] have shown that noise reduction in the order of 9 dB at the spectral peak is achieved by replacing the solid trailing edge of the surface with a permeable material. This is due to a better pressure balance between the upper and lower sides of the plate and a reduction in the spanwise pressure coherence at the plate trailing edge, which reduce the intensity of noise scattered at that region [19]. The amplitude of noise reduction is also connected to the properties of the permeable material such as porosity and permeability/resistivity, up to a certain threshold. However, for a partially porous surface, scattering still occurs at the solid-permeable junction, which becomes the location of the dominant acoustic source [19].

Those studies, however, have been performed with a simplified geometry, i.e. jet with a flat plate, and only the acoustic effect of permeable materials has been verified. Therefore, it is necessary to investigate if permeable materials are still a feasible solution in a realistic aircraft configuration and that they are not responsible for significant aerodynamic performance degradation, i.e. lift decrease and/or drag increase. Moreover, obtaining JIN reduction with a realistic geometry and at in-flight conditions is a challenging task, as reported by Mengle et al. [20]. The presence of the external flow is likely to reduce the acoustic benefits provided by the permeable materials, with respect to a static measurement condition.

In this work, wind tunnel measurements are performed with a half-model representative of a commercial aircraft, equipped with permeable deployed flaps. Permeability is achieved through perforations on the flap surface, connecting the lower and upper sides in a direction normal to the chord line. In order to minimize potential effects on performance, the perforations are restricted to a spanwise section in the vicinity of the jet flow. Acoustic measurements with a microphone phased array are performed in order to verify the noise reduction that can be achieved with such configuration, particularly in the presence of free-stream, representing a flight condition. Moreover, aerodynamic measurements with a force balance and a multi-hole pressure probe are carried out to study the effect of the permeable materials on the model lift and drag forces as well as the flow around the flaps.

This paper is organized as follows. In section 2, the experimental set-up is described, including the characteristics of the permeable flaps. In section 3, the results of the experiments are discussed, based on aerodynamic force data, flow-field mapping, beamforming maps and noise spectra. Finally, the conclusions of this work are summarized in section 4.

II. Experimental Set-up

A. Wind Tunnel Facility and Models

The experiments are performed in the Low-Speed Wind Tunnel (LST) at the German-Dutch Wind Tunnels (DNW) facility in Marknesse, The Netherlands. The LST is an atmospheric, closed-circuit wind tunnel with a working section of 5.75 m x 3.0 m x 2.25 m in length, width and height, respectively. It has a contraction ratio of 9, a maximum operating speed of 80 m/s and maximum non-uniformity of 0.2% of the flow speed.

A half model representative of a commercial aircraft is used for the measurements [21]. It comprises a half-fuselage and a wing with deployed flaps, as shown in Fig. 1a. A peniche of 30 mm thickness is also included below the half fuselage. No tail planes or slats have been considered since they are not relevant for jet-installation noise and would add complexity to the study. The model dimensions are shown in Fig. 1b. The flaps are deflected by 35°, which is representative of a landing condition, wherein the trailing edge is positioned the closest to the jet flow such that the JIN source is the strongest. A zig-zag trip is applied on the wing at a position of 3% of the local chord, whereas on the fuselage the trip was applied near the nose [21].

A separate nacelle piece is used to generate a single-stream jet flow from compressed air continuously supplied (maximum mass flow rate of 5 kg/s at 80 bar). The nacelle has a length of 1.1 m and an exit diameter D_j = 113 mm. The centerline is approximately aligned with the junction between inboard and outboard flaps at a height of 0.73 m from the tunnel floor. Moreover, the flap trailing edge at the nacelle centerline is positioned at an axial distance of $3.4D_j$ ($x-$axis) with respect to the nozzle exit plane, and a radial distance of $0.72D_j$ ($y-$axis) with respect to the nozzle centerline. The nacelle is mounted on an angled strut, attached to the tunnel floor, and there is no pylon connecting it to the airframe.

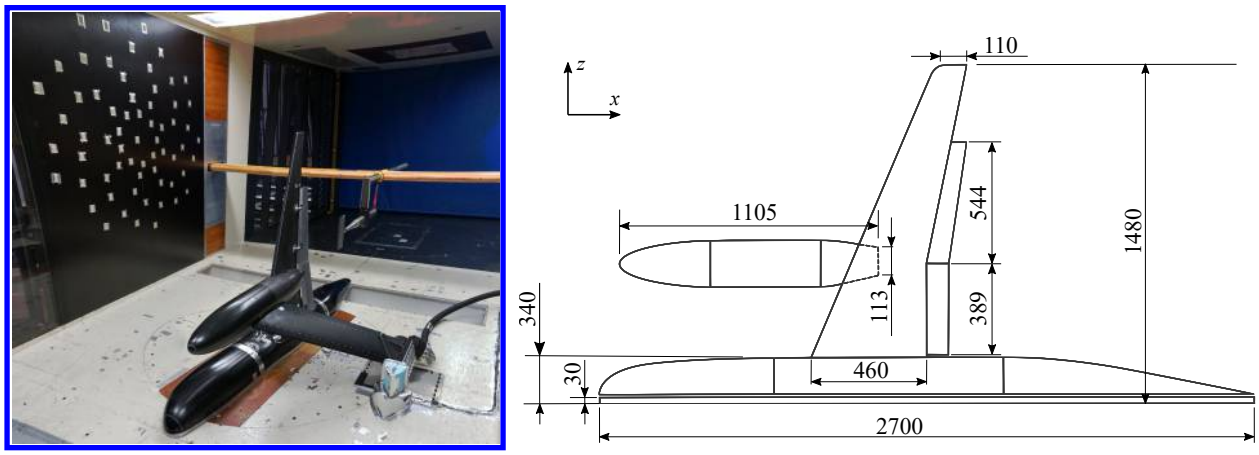

Fig. 1 (a) Model set-up in the wind tunnel, comprised by the fuselage, wing, deployed flaps and the nacelle. On the side wall, microphones are placed for acoustic measurements, whereas a wake rake is used for flow field mapping. (b) Main dimensions of the model in mm.

B. Permeable Flaps

The JIN reduction solutions studied in this work are partially permeable flaps, comprised by a perforated structure with straight channels normal to the flap chord line. In the chordwise direction, the perforations start at 25% of the flap chord in order to avoid flow communication between the upper and lower sides near the suction peak. In the spanwise direction, the perforations are placed near the junction between the inboard and outboard flaps, which approximately coincides with the jet centerline, and with a span of $1.5D_j$ (167 mm) at each flap. Near the flap tip (both inboard and outboard), there is a small region without perforations due to a manufacturing requirement. The perforations also avoid the bracket areas. The channels have a diameter of 0.8 mm and two different configurations in terms of hole spacing are investigated. The first one has a uniform spacing of 4 mm between channels at the same chordwise and spanwise rows, as shown in Fig. 2, and it is referred in this manuscript as UPF (uniform permeability flap).

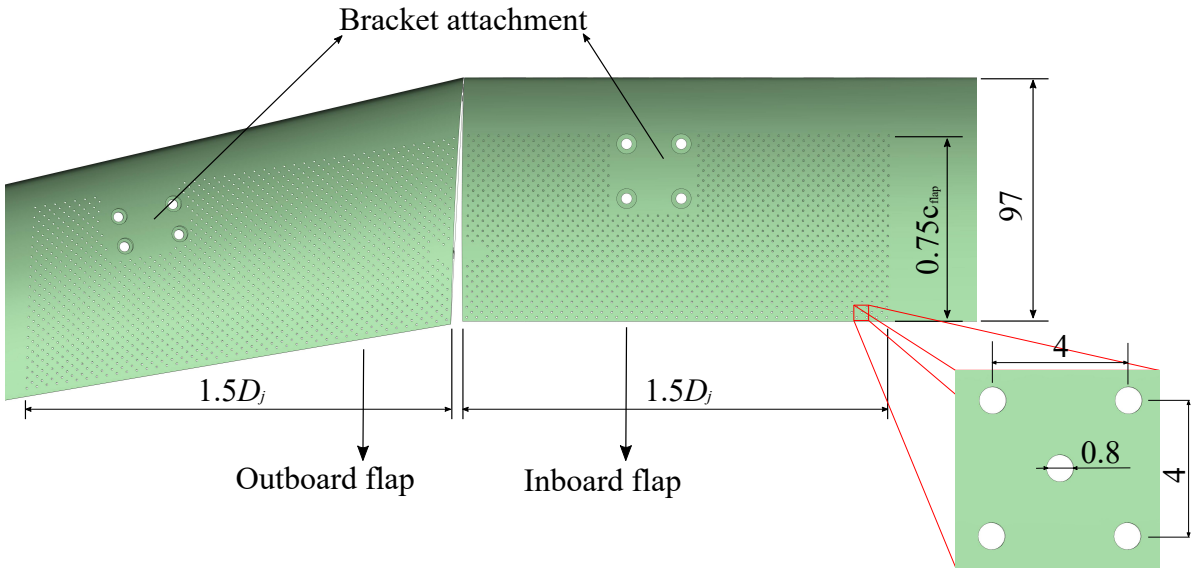

Fig. 2 Perforated flap with uniform permeability. The perforated region is restricted to the inboard-outboard flap junction, which is approximately coincident to the jet centerline. Dimensions in mm.

A second configuration comprises a permeability increase towards the flap trailing edge, obtained by progressively reducing the hole spacing (GPF - gradient permeability flap). This concept is investigated since it is hypothesized that it can provide additional aerodynamic and aeroacoustic benefits [19]. By increasing the hole spacing near the leading edge, it is likely that the effect of the permeable flap on lift and drag will be lower with respect to the uniform pattern. Moreover, a higher permeability at the trailing edge can lead to lower noise emission since this is the region where the source is the strongest. Finally, with a smooth change in surface impedance from the solid to the permeable regions, it is believed that junction scattering effects can be mitigated [18].

In order for the two cases to be comparable, the integral permeability of the perforated structure must be the same. Therefore, the hole spacing of the GPF has been designed to match the integral permeability of the UPF. Moreover, instead of having alternating rows with the holes in an X-pattern, this configuration has a logarithmic increase in hole spacing in the streamwise direction, from 1.6 mm to 3.2 mm from trailing edge to leading edge. In the spanwise direction, the hole spacing also increases towards the trailing edge, but it is constant within each row. For the first row, the hole spacing is 6.4 mm, whereas for the last one (at the trailing edge) it is 3.2 mm. This decrease in spacing also follows a logarithmic pattern. The higher hole spacing in the spanwise direction with respect to the streamwise one has been chosen since pressure fluctuations caused by the jet on the flap surface are the strongest near the centerline (inboard-outboard flap junction). Thus, it is not necessary to have a high permeability away from this region. The GPF concept is shown in Fig. 3.

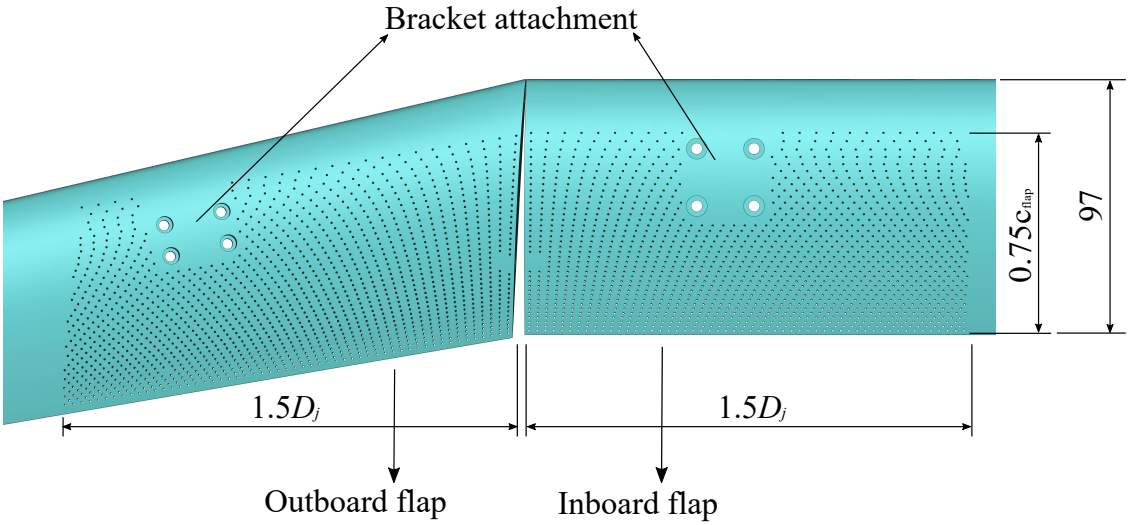

Fig. 3 Perforated flap with gradient permeability. Dimensions in mm.

The porosity (σ) of each configuration, defined as the ratio between the volume of the permeable flaps (V_p) with respect to the baseline solid one (V_s), as shown in Eq. (1), is reported in Table 1. It is shown that the porosity values between the UPF and GPF configurations are similar, which is a necessary condition to obtain the same permeability.

$$\sigma = 1 - \frac{V_p}{V_s}. \tag{1}$$

Table 1 Porosity values for each permeable flap configuration.

	σ [%]
UPF - Inboard	1.89
UPF - Outboard	2.00
GPF - Inboard	1.73
GPF - Outboard	1.87

In order to verify that both concepts have similar integral permeability, the approach reported by Rubio Carpio et al. [22] is applied. The local permeability of the GPF in the streamwise direction is computed based on the hole spacing at each row and plotted in Fig. 4. The integral of the curves yields an overall permeability $K_{\mathrm{UPF}} = 6.82 \times 10^{-10}$ and $K_{\mathrm{GPF}} = 7.23 \times 10^{-10}$. A similar trend is obtained by computing the spanwise permeability for each row. Therefore, it is verified that the two permeable flap concepts have similar overall properties and the main difference between them is the hole pattern.

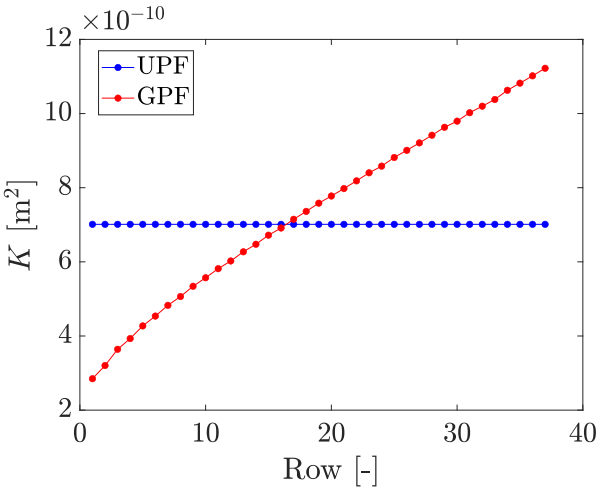

Fig. 4 Local permeability of the uniform and gradient flap concepts.

C. Instrumentation and Measurement Techniques

1. Aerodynamic Measurements

The model is mounted on a turntable on the floor and attached to a balance for aerodynamic force measurements. The three force components and moments are measured, although only the lift and drag are considered for the comparison between solid and permeable flaps. The maximum loads that can be withstood by the balance are 20 kN in the normal direction, 2 kN in the axial direction and 1.5 kNm of pitching moment, with uncertainties of 4 N, 2.5 N and 2 Nm, respectively. Since the nacelle is not attached to the model, it has been removed during the force balance measurements, which are carried out for a jet-off condition.

Flow-field measurements are also carried out in order to investigate the effect of the permeable flaps on the wake of the model and possibly even on the jet flow itself. Therefore, the measurements are performed downstream of the model with a rake of 18 5-hole pressure probes (see Fig. 1a) in order to obtain the 3 flow velocity components. The probes are spaced by 15 mm and thus the total length of the rake is 255 mm. They are connected to a 64-port ESP ZOC Scanivalve module with a differential pressure range of 5 psi and an uncertainty of 0.1% of this range. Regarding the measured quantities, the following uncertainty values are obtained: local incidence angle $\leq 0.2°$, sideslip angle $\leq 0.2°$, Mach number ≤ 0.02, and total pressure $\leq 2\%$.

A $yz-$plane, located $6D_j$ downstream of the nozzle exit, is chosen for the measurements. It is centered at the nozzle centerline with dimensions of 500 mm x 500 mm. The measurements are carried out in 2 sweeps in the $y-$direction with a 7 mm spacing between points; in the $z-$direction the point spacing is the same as the probe spacing of 15 mm. This plane includes the wake of the wing/flap and an axial section of the jet flow. By comparing the velocity components for each configuration, it can be assessed how the permeable flaps affect the flow around the wing, and the results can be linked to the aerodynamic forces measured with the balance.

The jet velocity is measured and controlled via pressure and temperature probes placed inside the nozzle. The former are connected to the ESP ZOC Scanivalve module, similarly as the multi-hole probes, whereas the latter are connected to a TempPoint measurement system with a maximum uncertainty of 1 K. The aerodynamic measurements are performed for a free-stream velocity of 60 m/s ($M_f = 0.18$) and a nominal jet velocity of 170 m/s ($M_j = 0.5$) for the three geometric configurations. The Reynolds number based on the free-stream velocity and the mean aerodynamic chord of the model is $Re_f = 1.4 \times 10^6$, whereas the one based on the nozzle exit diameter and the jet speed is $Re_j = 1.29 \times 10^6$.

2. Acoustic Measurements

The acoustic measurements are carried out with a microphone phased array mounted on a side wall of the working section. Due to the presence of the nozzle strut, which can reflect and diffract acoustic waves propagating from the source of interest to the microphones, the array has been mounted facing the upper side of the model (shielded side of the jet). This configuration still allows for jet-installation noise measurements since the source of interest is located at the flap trailing edge and it is not subjected to shielding effects.

The phased array comprises 64 G.R.A.S. 40PH free-field microphones (frequency response: ± 1 dB; frequency range: 10 Hz to 20 kHz; maximum output: 135 dB, ref. 2×10^{-5} Pa) with integrated CCP pre-amplifiers. The microphones are arranged in an optimized multi-arm spiral configuration [23, 24], as shown in Fig. 5. The effective diameters in the $x-$ and $z-$directions are 2 m and 1.5 m, respectively. In order to mitigate spurious noise due to the tunnel boundary layer, the microphones are recessed 5 mm in the wall and the cavities are covered with Kevlar patches, as shown in Fig. 1a.

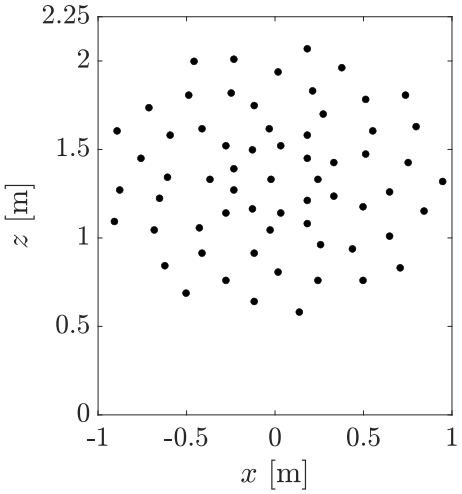

Fig. 5 Microphone positions in the phased array.

The acquisition is performed with a sampling frequency of 51.2 kHz for 60 seconds and the recorded signals are used for acoustic source localization using Conventional Frequency-Domain Beamforming [25]. In order to compute the Cross-Spectral Matrix (CSM), the signals are divided into blocks of 1024 samples and windowed with a Hanning weighing function, with a 50% overlap; the CSMs obtained from each block are then averaged. The source maps are constructed on a scan plane parallel to the array, at the trailing-edge position of the junction between the inboard and outboard flaps (y = 1.59 m). The scan plane dimensions are 3.2 m x 2.25 m, which corresponds to the extension of the model in the $x-$ direction and the full height of the tunnel, subdivided into grid elements of 16 mm x 12 mm (200 grid elements in each direction). Afterwards, the narrowband noise spectra are obtained via the source power integration method [26, 27] applied to a region of interest (ROI) at the flap trailing-edge, and plotted with a frequency band of 50 Hz. This ROI has dimensions of 1 m x 1 m, centered at the source on the flap trailing edge. The acoustic measurements are carried out for a jet velocity of $M_j = 0.50$ and different free-stream conditions, both static ($M_f = 0$) and flight ($M_f = 0.09$ and $M_f = 0.18$) for an angle of attack $\alpha = 0°$. The parameters for each measurement type are summarized in Table 2.

Table 2 Flow parameters for each measurement type.

Measurement Type	M_j [-]	M_f [-]	α [°]
Force Balance	0.5	0.18	0 - 12
Flow-field Mapping	0.5	0.18	0
Acoustic	0.5	0 / 0.09 / 0.18	0

III. Results and Discussion

A. Aerodynamic Forces

The aerodynamic forces are analyzed in this section for the different flap configurations, as shown in Fig. 6 in terms of coefficients non-dimensionalized by the free-stream dynamic pressure and the wing planform area.

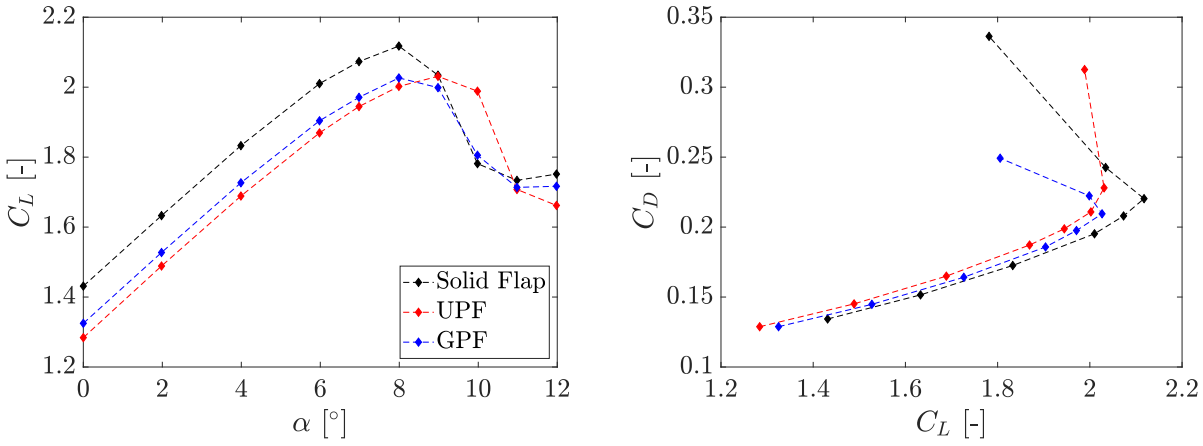

Fig. 6 (a) Lift coefficient curve for the baseline solid flap and permeable configurations (b) Drag polar curve for the baseline solid flap and permeable configurations.

The results in Fig. 6a show that permeable flaps cause lift reduction throughout the whole range of measured angles of attack. Lift coefficient values for specific angles are reported in Table 3. For $\alpha = 0°$, the UPF is responsible for a C_L reduction in the order of 11% with respect to the baseline solid case, whereas for the GPF, the reduction at this angle is in the order of 7% likely due to a lower permeability near the flap suction peak where most of the lift is generated. Since these measurements are performed without the jet flow, this behaviour is thus linked to permeability effects on the flow around the flap. As the angle of attack is increased, the difference relative to the baseline is slightly reduced. For the solid flap, $C_{L_{\max}}$ is reached for $\alpha = 8°$; at this angle, the UPF results in a 6% lift reduction, whereas the GPF result in 4% decrease. There is also a shift in the angle of maximum lift for the UPF, possibly caused by delayed boundary-layer separation at that angle. Further research into this behavior is necessary.

In terms of drag force, the permeable flaps have a lower impact; the C_D values for the UPF and GPF are lower than that of the baseline case, as reported in Table 3, which can be related to the lift decrease caused by the flow communication between upper and lower sides (reduction of induced drag). Therefore, the drag polar, shown in Fig. 6b, is plotted as a function of the measured lift coefficient for each case. Both permeable flaps result in higher drag values with respect to the baseline solid configuration, with the GPF providing a lower penalty than the UPF. By fitting the pre-stall region of the curves (considering $C_L < 2$) with a second order polynomial, and targeting the lift coefficient of the baseline case for $\alpha = 0°$ ($C_L = 1.43$), it is found that the UPF results in 3% drag augmentation, whereas for the GPF the increase is only of 0.5%.

Table 3 Lift and drag coefficients for the three investigated flap configurations, at two different angles of attack.

Flap Configuration	C_L [-]		C_D [-]	
	$\alpha = 0°$	$\alpha = 8°$	$\alpha = 0°$	$\alpha = 8°$
Solid	1.431	2.117	0.1343	0.2203
UPF	1.284	2.002	0.1287	0.2108
GPF	1.325	2.026	0.1288	0.2095

B. Flow Field

Flow-field maps are obtained from the 5-hole probe measurements downstream of the model, which allow for an assessment of the effect of the permeable flaps on the model wake and jet development. The contour plots in Fig. 7 show the time-averaged velocity component u (in the $x-$direction), non-dimensionalized by the free-stream speed, at a plane located $6D_j$ downstream of the nozzle exit, for the three flap configurations. The central region, corresponding to the jet flow, is slightly saturated in order to allow sufficient visibility of the model wake. The horizontal dotted lines correspond to regions where the velocity profiles are plotted for the three configurations.

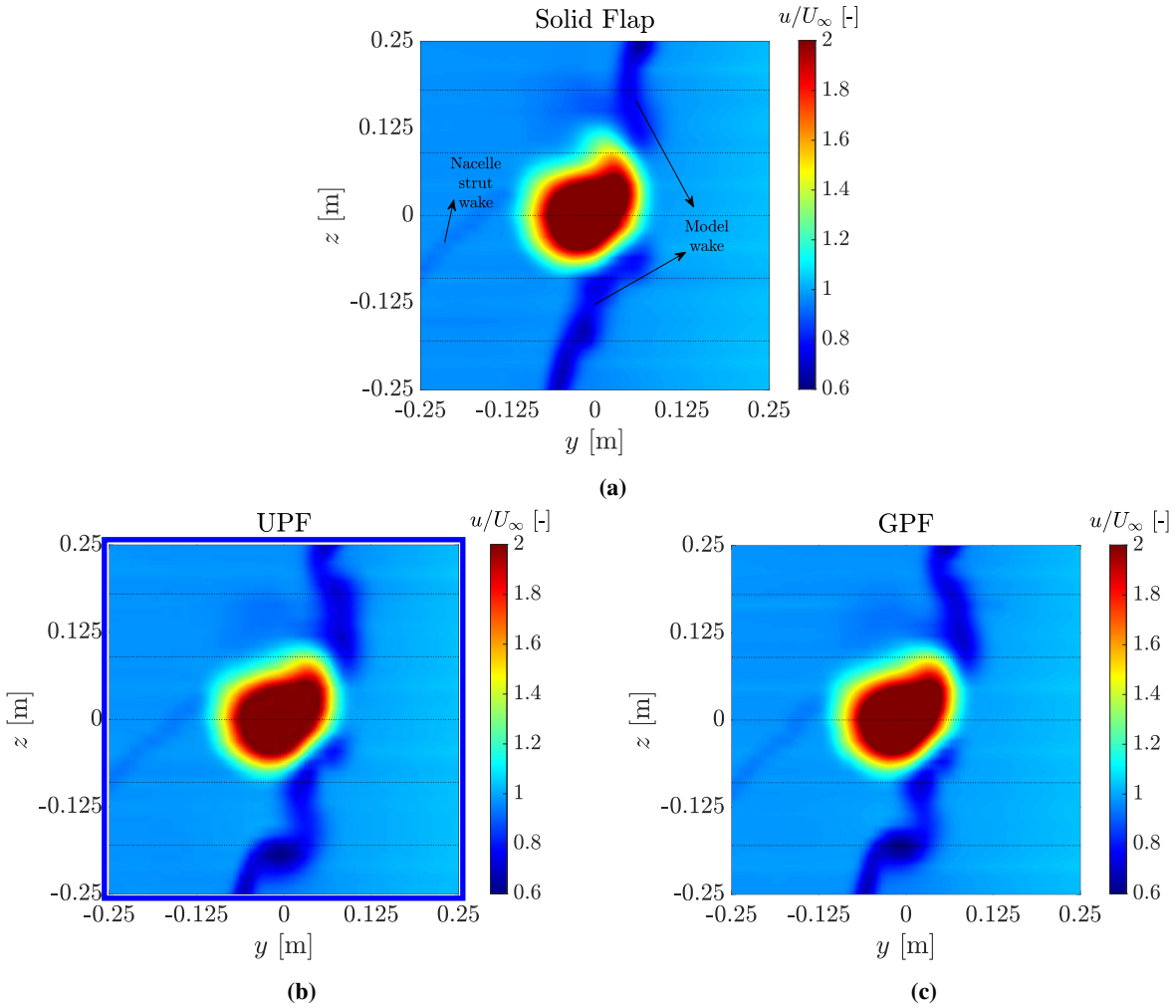

Fig. 7 Flow-field maps of the velocity component u at a $yz-$plane located $6D_j$ downstream of the nozzle exit. (a) Baseline solid flap. (b) Uniform permeability flap. (c) Gradient permeability flap. The dotted lines correspond to stations where the velocity profiles are extracted.

In Fig. 7a, for the solid flap case, the high velocity region of the jet flow is clearly distinguished in the center. On the left-hand side of the plot, the nacelle strut wake is slightly visible, although it does not seem to affect the jet or the model wake. The jet, however, does not display a round shape likely due to impingement on the wing/flap as well as due to the velocity induced by the wing in the negative $y-$direction.

For the permeable flaps, the velocity in the model wake is visibly lower than that of the solid one, particularly in the region 0.1 m $< z <$ 0.2 m. Moreover, a very low-velocity region occurs at $z = -0.18$ m resembling a strong vortex. For a quantitative comparison between the three configurations, the velocity profiles in the regions corresponding to the black dotted lines are plotted in Fig. 8.

Starting from the upper side, the profiles at $z = 0.18$ m are shown in Fig. 8a. For the permeable flaps, the wake velocity deficit is higher than that of the solid one. Moreover, the region of lowest velocity is located to the right-hand

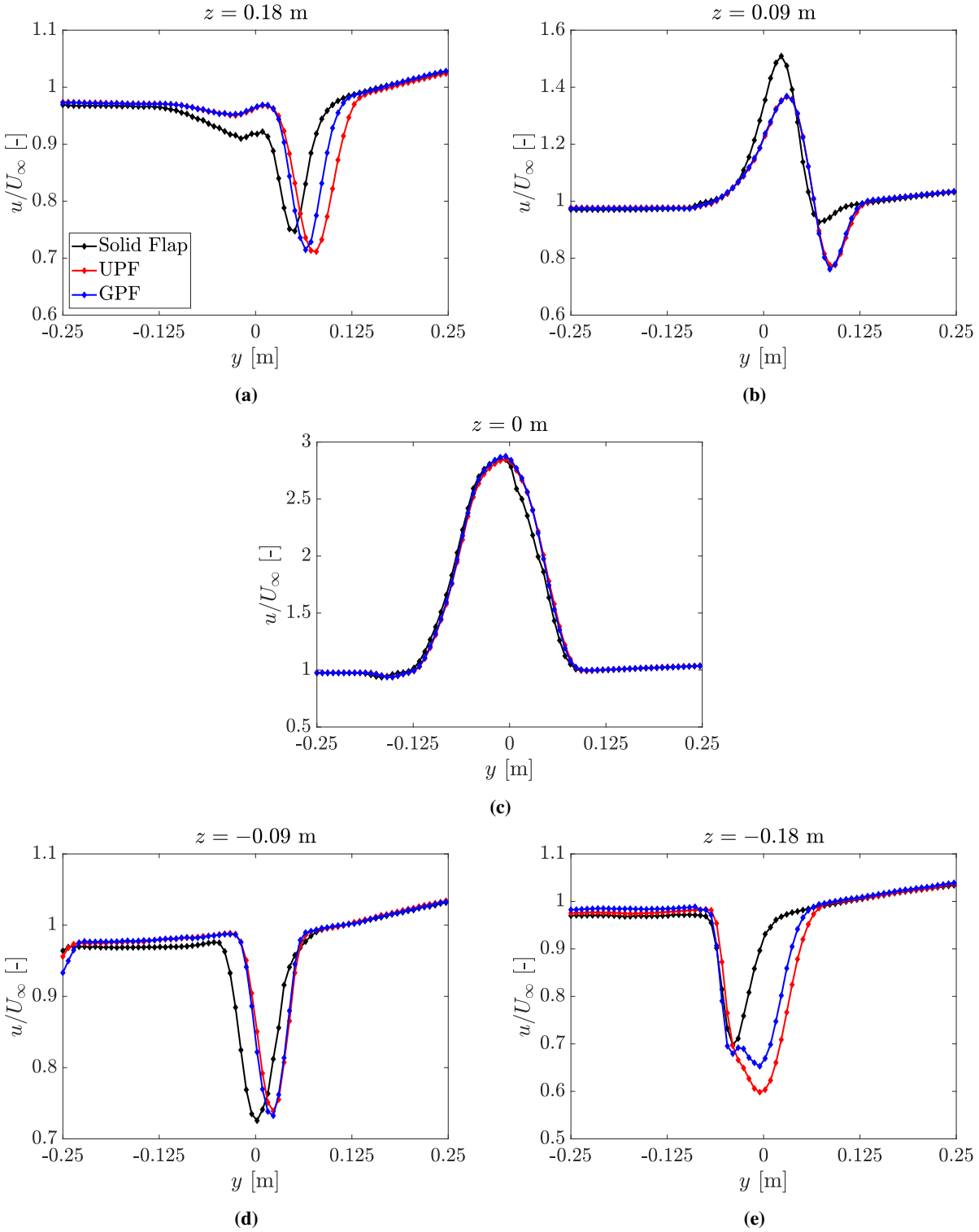

Fig. 8 Profiles of $u-$velocity at five spanwise stations, displaying the model wake and the jet flow for the three flap configurations. (a) $z = 0.18$ m. (b) $z = 0.09$ m. (c) $z = 0$ m (d) $z = -0.09$ m (e) $z = -0.18$ m

side with respect to the solid case, showing that the wake of the former does not have a strong downward velocity component. This is likely due to either flow separation caused by the communication between the upper and lower sides

of the flap or an effective reduction of the local angle of attack. This behaviour is more noticeable for the UPF, which has a higher permeability near the leading edge.

A similar behaviour is shown for $z = 0.09$ m in Fig. 8b, with the maximum velocity deficit at $y \approx 0.1$ m for the permeable cases, which does not occur for the solid one. Moreover, the higher velocity near $y = 0$ indicates the presence of the steady jet flow, although the velocity amplitude for the permeable cases is lower, likely due to interaction with a stronger model wake. For $z = 0$, shown in Fig. 8c, no visible wake region is detected since this position corresponds approximately to the jet centerline and the velocity amplitude is still approximately the nominal jet one ($M_j = 0.5$ or $2.83U_\infty$). A slight asymmetry is shown for the solid case, with slightly lower values in the positive $y-$direction. This is believed to be due to a region of jet impingement on the flaps, which block a small part of the flow in that direction.

The profiles at $z = -0.09$ m, shown in Fig. 8d display the same characteristics of those from Fig. 8a. However, the profiles at Fig. 8e show a much wider wake for the permeable flaps, with a clearly higher integral velocity deficit. Moreover, the wakes do not appear to be symmetric in y, indicating the occurrence of an additional phenomenon. From the maps in Fig. 7, the flow in this region appears to be similar to a vortex. Therefore, it is useful to compute the flow vorticity ω in the x-direction, as plotted in Fig. 9.

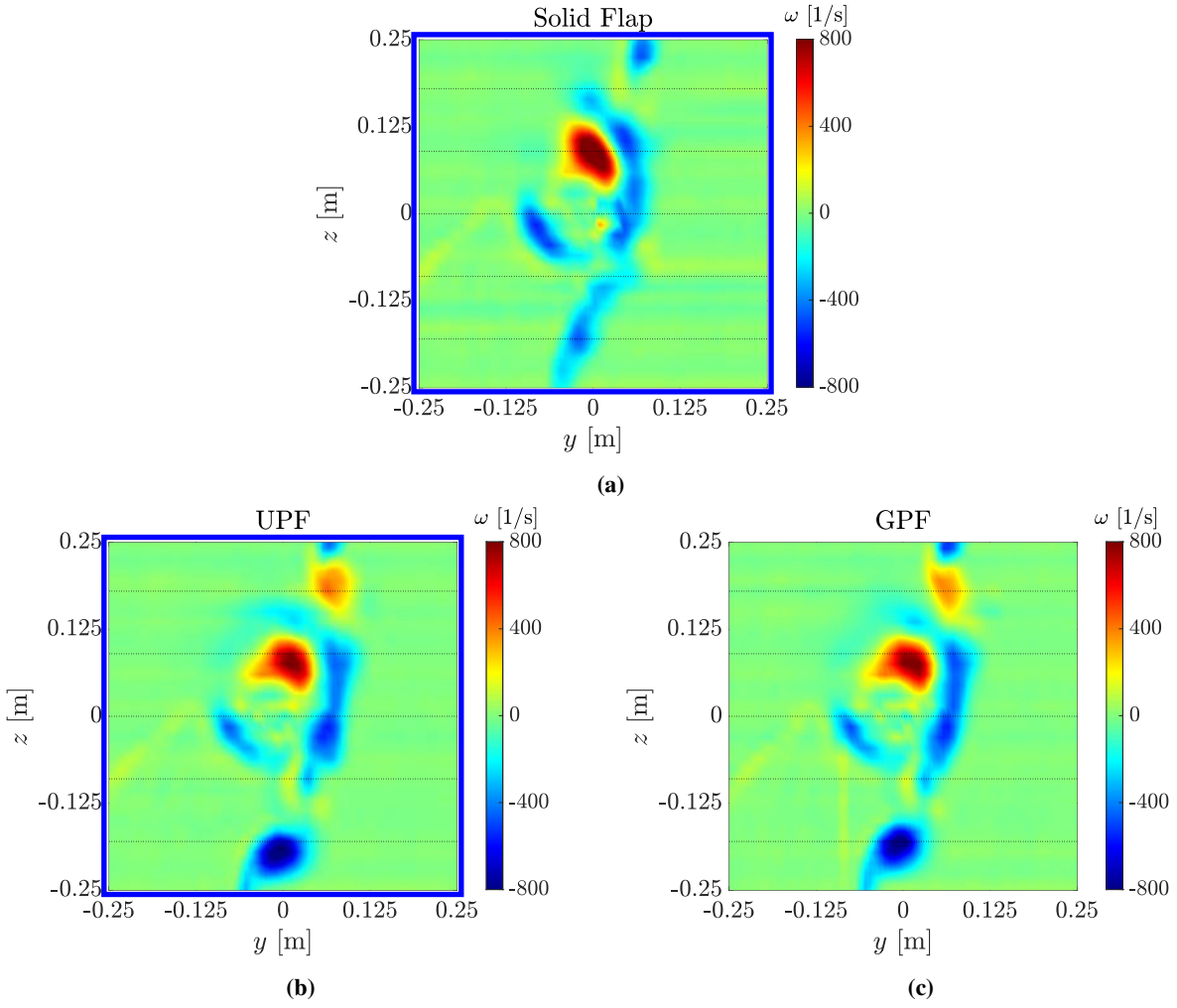

Fig. 9 Flow-field maps of the vorticity ω in the $x-$direction. (a) Baseline solid flap. (b) Uniform permeability flap. (c) Gradient permeability flap.

The high vorticity in the central region of the plots corresponds to the mixing layer of the jet and it displays similar values for all three configurations. However, for $z = -0.18$ m, a strong vortex is visible in the plots for the permeable flaps. Nevertheless, the origin of this vortex are unclear. It is hypothesized that a flow structure similar to a side-edge vortex is formed in the spanwise region where permeability starts. This hypothesis is reinforced by the position of the

vortex approximately coinciding with that of the spanwise solid-permeable junction. A strong vorticity region also occurs at the outboard side ($z = 0.18$ m) of the permeable flaps, once again near the end of the porous section in the spanwise direction, further increasing the likelihood of the side-edge vortex hypothesis. The higher vorticity at the inboard side can be linked to a higher flow circulation near the root of the wing with respect to a section closer to the tip. These vortices also likely have a significant contribution to the lift reduction measured for these configurations, as reported in the previous section. Further research into the possible generation of these vortices and their impact is necessary.

C. Beamforming Maps and Noise Spectra

In this section, the acoustic results from the phased array measurements coupled with the beamforming technique are discussed. The source maps for the three flap configurations are plotted in Fig. 10 for a frequency $f = 700$ Hz, corresponding to $St = 0.47$ ($St_j = f \times D_j/U_j$). The maps are obtained for $M_j = 0.5$ and $M_f = 0.18$.

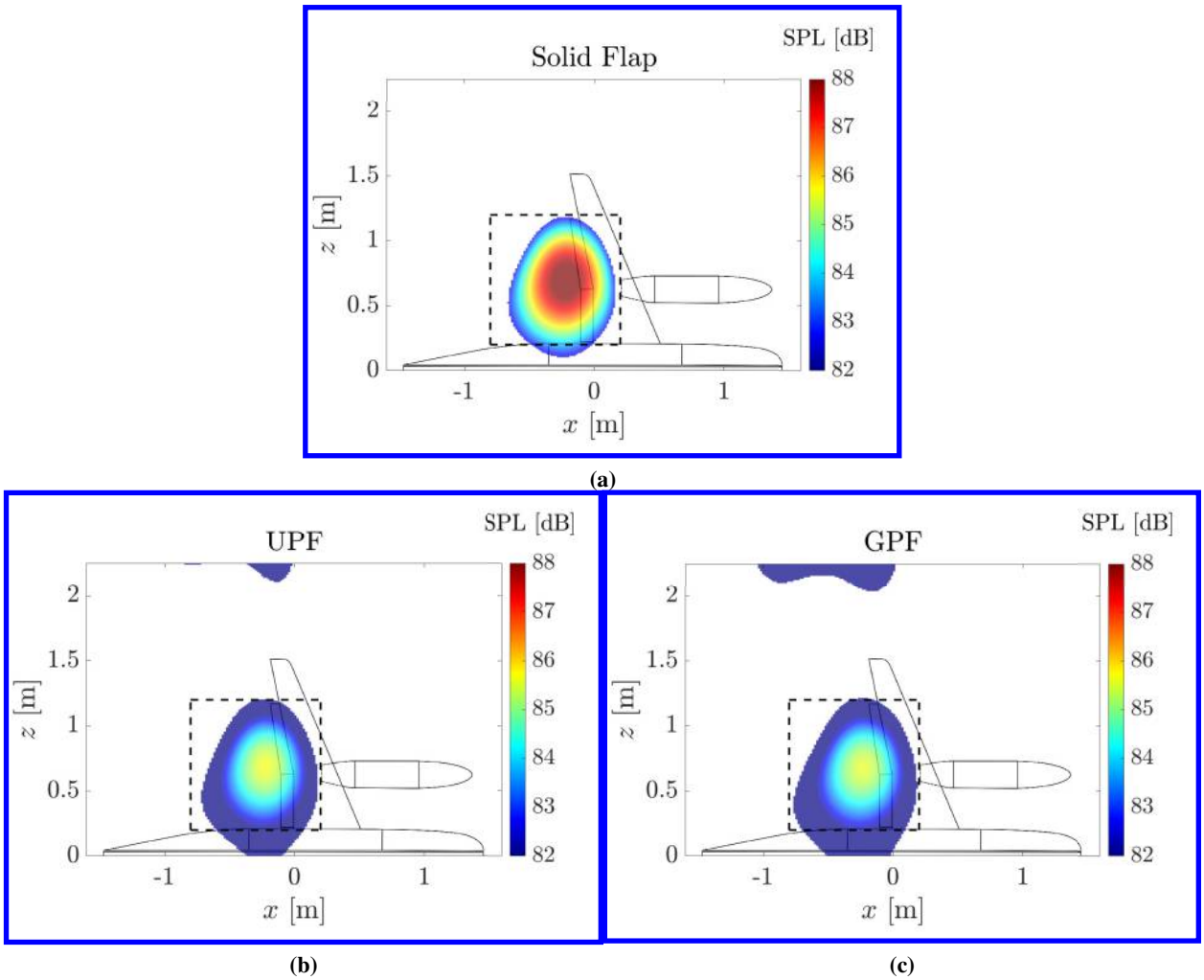

Fig. 10 Acoustic source maps obtained from beamforming for a frequency $f = 700$ Hz ($St_j = 0.47$). (a) Baseline solid flap. (b) Uniform permeability flap. (c) Gradient permeability flap. The dashed section corresponds to the region-of-interest, wherein source power integration is applied.

The beamforming maps show that the dominant acoustic source at this frequency is located near the flap trailing edge and approximately centered at the nozzle centerline, indicating that it occurs due to the interaction between the flap and the jet flow. For a jet-off condition, this source is not present in the beamforming maps, which in turn are dominated by the tunnel background noise and thus not shown. For all three flap configurations, the source is located at the same

position but with a lower amplitude for the permeable cases. For the baseline solid case, the peak source amplitude, in terms of Sound Pressure Level (SPL), is approximately 88.5 dB, whereas both the UPF and GPF have maximum amplitudes of 85.5 dB. No significant differences are visible between the permeable cases. Therefore, it is shown that the permeable flaps are effective in reducing JIN in flight conditions.

In order to verify the effect of the permeable flaps at different frequencies, SPL spectra are computed using the source power integration technique [26, 27] applied to the region delimited by the dashed lines in Fig. 10. Thus, the results focus on the flap trailing-edge source and the effect of spurious sources is mitigated. The spectra are plotted for a minimum frequency of 300 Hz, below which the tunnel background noise is dominant, and a maximum of 4 kHz, wherein the presence of sidelobes and spurious sources from the tunnel and nozzle in the beamforming maps reduce the accuracy of the analysis.

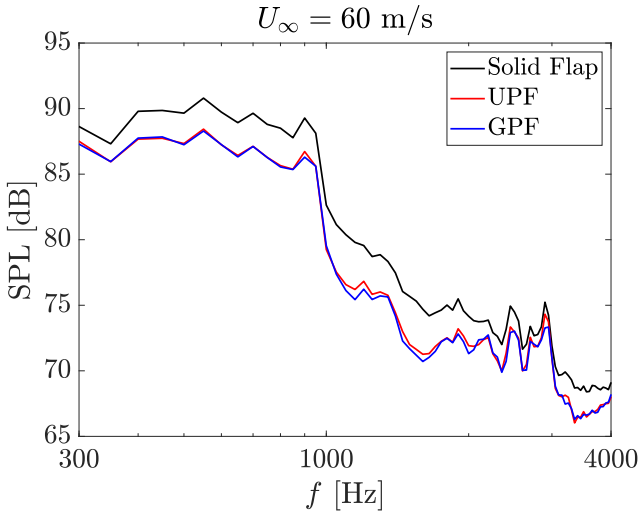

Fig. 11 SPL spectra obtained from source power integration applied to the flap trailing-edge region for all three configurations.

The spectra show that the permeable flaps provide noise reduction in a wide range of frequencies. For 400 Hz $< f <$ 1000 Hz, both the UPF and the GPF have lower SPL than the baseline solid case, with an approximately constant reduction of 3 dB in this range. The sharp drop occurring at approximately 1000 Hz is typical when only the trailing-edge source is considered, while disregarding the contribution by turbulence mixing [8]. Moreover, both permeable flap configurations have similar noise amplitudes throughout the entire frequency range analyzed. Therefore, it is likely that the hole placement does not play a large role in the amplitude of the trailing-edge source, or it is not as significant as the integral permeability of the structure.

The effect of free-stream on the JIN levels and the relative reduction provided by the permeable flaps is assessed by plotting the SPL spectra for different free-stream speeds, as shown in Fig. 12.

The results for the static condition ($U_\infty = 0$) are plotted in 12a. Initially, it is shown that the noise levels for the solid flap case are higher than those reported in Fig. 11 for the same case. For a frequency of 900 Hz, for example, the SPL for the static case is approximately 94 dB, whereas with a free-stream speed of 60 m/s, the noise levels are 89.3 dB. This occurs because in the presence of free-stream the shear stresses in the jet mixing-layer are lower with respect to the static condition, thus reducing the amplitude of the velocity and pressure fluctuations prior to their scattering at the flap trailing edge. This is further verified by intermediary SPL values obtained with a free-stream speed of 30 m/s, as shown in Fig. 12b and reported in Table 4. For the permeable flaps, on the other hand, the noise levels are less sensitive to the free-stream speed, as reported in Table 4 as well. This is likely due to a reduced sensitivity of the dominant source to the amplitude of impinging pressure fluctuations [18]. Due to the flow communication between the upper and lower sides of the flap, there is a weaker pressure imbalance at the flap trailing edge, which in turn plays a relatively lower role in the produced noise levels with respect to the solid case.

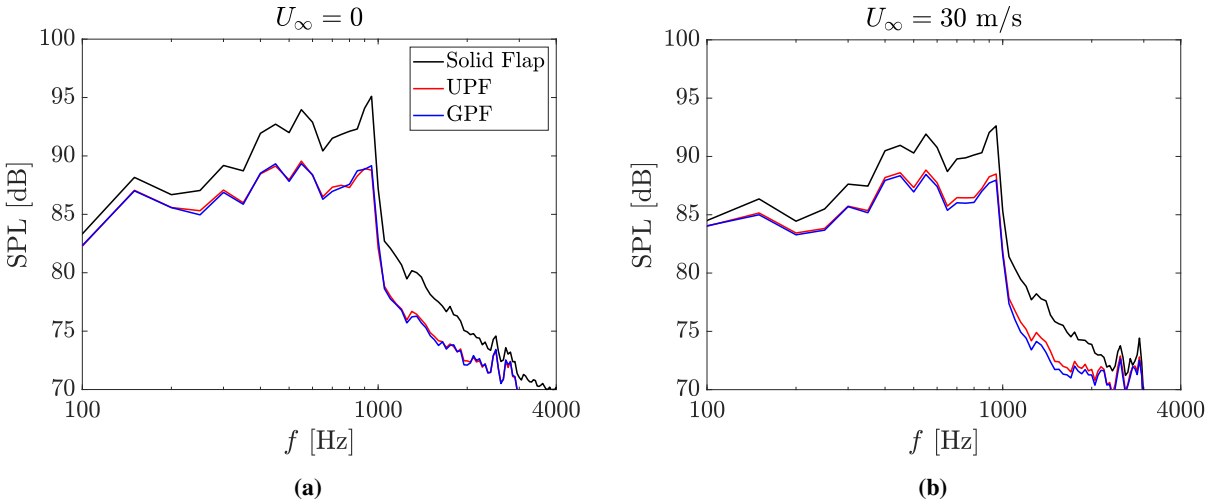

Fig. 12 SPL spectra obtained from source power integration applied to the flap trailing-edge region for all three configurations at different free-stream speeds. (a) $U_\infty = 0$**. (b)** $U_\infty = 30$ **m/s.**

Table 4 SPL obtained from the noise spectra for the three flap configurations at different free-stream speeds for a frequency $f = 900$ **Hz.**

	$U_\infty = 0$	$U_\infty = 30$ m/s	$U_\infty = 60$ m/s
Solid Flap	94.0	92.0	89.3
UPF	88.9	88.2	86.7
GPF	88.8	87.7	86.3

IV. Conclusions

An experimental investigation on jet-installation noise reduction with the application of permeable flaps is performed. A half-model representative of a commercial aircraft with flaps deployed in a landing configuration is selected for the tests. A separate nozzle is included for generating the jet flow in the vicinity of the airframe.

Acoustic results obtained from phased array microphone measurements show a clear source at the flap trailing edge, approximately centered at the nozzle centerline, caused by interaction with the jet flow. With the permeable flaps, the source position remains unchanged, but a clear reduction in amplitude, in the order of 3 dB is verified. The noise reduction provided by the permeable flaps is consistent in the entire frequency range where JIN is the dominant source, and thus it is concluded that they are effective noise reduction solutions. For a static condition, without free-stream, the noise reduction provided by the permeable flaps reaches 5 dB due to the higher amplitude of pressure fluctuations in the jet mixing layer for this condition.

Aerodynamic force measurements carried out with a balance show that the permeable flaps are responsible for a lift reduction in the order of 7% at zero degree angle of attack. This is due to the flow communication between the upper and lower sides of the flap, which are likely to alter the boundary layer properties on the surface due to the pressure gradient between the two sides. In terms of drag, the permeable flaps result in only a minor increase for a similar lift coefficient, with respect to the baseline configuration. Comparing the two permeable cases, the gradient permeability flap outperforms the uniform one, likely due to a lower permeability near the flap suction peak, where most of the lift is generated. In the studied configuration with a high flap deflection, it is expected that this effect is the strongest. For a take-off condition, wherein a lift decrease would be more harmful, the permeable flaps would have a lower impact on the aerodynamic performance due to a lower deflection angle and thus lower pressure differential between the upper and lower surfaces.

Flow velocity maps show that the permeable flaps generate a stronger wake than their solid counterpart. This is possibly due to boundary-layer separation occurring due to the communication between the upper and lower sides of the flap, which introduces a flow component normal to the chord. Therefore, the wake velocity deficit is higher and the

downward induced velocity by the wing is not as significant with respect to the solid case, thus likely the cause for the lower lift force. Additionally, vorticity maps reveal the presence of two large vortices near the spanwise regions where the perforations start at both inboard and outboard sides. It is believed that the perforations produce a flow structure similar to a side-edge vortex, which can be also responsible for a portion of the aerodynamic penalties reported since these vortices reduce the local angle of attack and, consequently, the generated lift.

It is shown that the permeable flaps are able to significantly reduce jet-installation noise for an aircraft configuration in flight conditions. It has been also shown that the aerodynamic penalties (lift decrease and drag increase) caused by the permeable flaps can be mitigated by defining a proper hole placement on the structure; by introducing a gradient permeability, for example, an equal noise reduction as provided by an uniform permeability can be obtained with lower performance degradation. Therefore, with an optimization of this parameter both in the streamwise and spanwise directions, considering the pressure fluctuations on the flap surface, for example, a permeable flap is a feasible JIN reduction solution both in terms of acoustics and performance.

Acknowledgments

This work is part of the IPER-MAN project (Innovative PERmeable Materials for Airfoil Noise Reduction), project number 15452, funded by the Netherlands Organization for Scientific Research (NWO). The authors would like to thank Prof. Georg Eitelberg from TU-Delft and Ir. Koen Artois from DNW for the support in the preparation and planning of the wind tunnel tests. The authors would also like to thank Ir. Steve van Herk and Ing. Frank Schilder from DEMO at TU-Delft for the mechanical design and production of the permeable flaps. The authors would also like to thank all DNW personnel involved in the preparation and execution of the wind tunnel tests. Finally, the authors would also like to thank Prof. Mirjam Snellen and Prof. Sybrand van der Zwaag from TU-Delft, for collaboration in the project.

References

[1] Huff, D. L., "Noise Reduction Technologies for Turbofan Engines," *NASA/TM—2007-214495*, 2007, pp. 1–17.

[2] SenGupta, G., "Analysis of Jet-Airframe Interaction Noise," *8th AlAA Aeroacoustics Conference*, Atlanta, GA, USA, 1983.

[3] Brown, W. H., and Ahuja, K. K., "Jet and Wing/Flap Interaction Noise," *AIAA/NASA 9th Aeroacoustics Conference*, WiIIiamsburg, VA, USA, 1984. https://doi.org/10.2514/6.1984-2362.

[4] Casalino, D., and Hazir, A., "Lattice Boltzmann Based Aeroacoustic Simulation of Turbofan Noise Installation Effects," *23rd International Congress on Sound & Vibration*, Athens, Greece, 2014, pp. 1–8.

[5] Hughes, C., "The Promise and Challenges of Ultra High Bypass Ratio Engine Technology and Integration," *AIAA Aerospace Sciences Meeting*, Orlando, FL, USA, 2011.

[6] Head, R. W., and Fisher, M. J., "Jet/Surface Interaction Noise: - Analysis of Farfield Low Frequency Augmentations of Jet Noise due to the Presence of a Solid Shield," *3rd AIAA Aeroacoustics Conference*, Palo Alto, CA, USA, 1976. https://doi.org/10.2514/6.1976-502.

[7] Belyaev, I., Faranosov, G., Ostrikov, N., and Paranin, G., "A parametric experimental study of jet-flap interaction noise for a realistic small-scale swept wing model," *21st AIAA/CEAS Aeroacoustics Conference*, Dallas, TX, USA, 2015. https://doi.org/10.2514/6.2015-2690.

[8] Rego, L., Avallone, F., Ragni, D., and Casalino, D., "Jet-installation noise and near-field characteristics of jet-surface interaction," *Journal of Fluid Mechanics*, Vol. 895, 2020. https://doi.org/10.1017/jfm.2020.294.

[9] Cavalieri, A. V. G., Jordan, P., Wolf, W. R., and Gervais, Y., "Scattering of wavepackets by a flat plate in the vicinity of a turbulent jet," *Journal of Sound and Vibration*, Vol. 333, No. 24, 2014, pp. 6516–6531. https://doi.org/10.1016/j.jsv.2014.07.029.

[10] Papamoschou, D., "Prediction of Jet Noise Shielding," *48th AIAA Aerospace Sciences Meeting Including the New Horizons Forum and Aerospace Exposition*, Orlando, FL, USA, 2010. https://doi.org/10.2514/6.2010-653.

[11] Geyer, T., and Sarradj, E., "Trailing edge noise of partially porous airfoils," *20th AIAA/CEAS Aeroacoustics Conference*, Atlanta, GA, USA, 2014. https://doi.org/10.2514/6.2014-3039.

[12] Herr, M., Rossignol, K., Delfs, J., Lippitz, N., and Mößner, M., "Specification of Porous Materials for Low-Noise Trailing-Edge Applications," *20th AIAA/CEAS Aeroacoustics Conference*, Atlanta, GA, USA, 2014. https://doi.org/10.2514/6.2014-3041.

[13] Rubio Carpio, A., Avallone, F., and Ragni, D., "On the Role of the Flow Permeability of Metal Foams on Trailing Edge Noise Reduction," *2018 AIAA/CEAS Aeroacoustics Conference*, 2018. https://doi.org/10.2514/6.2018-2964.

[14] Teruna, C., Avallone, F., Ragni, D., Rubio-Carpio, A., and Casalino, D., "Numerical analysis of a 3-D printed porous trailing edge for broadband noise reduction," *Journal of Fluid Mechanics*, Vol. 926, 2021, p. A17. https://doi.org/10.1017/jfm.2021.704, URL https://www.cambridge.org/core/product/identifier/S0022112021007047/type/journal_article.

[15] Roger, M., Schram, C., and de Santana, L., "Reduction of airfoil turbulence-impingement noise by means of leading-edge serrations and/or porous materials," *19th AIAA/CEAS Aeroacoustics Conference*, 2013, p. 105. https://doi.org/10.2514/6.2013-2108.

[16] Geyer, T. F., Lucius, A., Schrödter, M., Schneider, M., and Sarradj, E., "Reduction of Turbulence Interaction Noise Through Airfoils With Perforated Leading Edges," *Acta Acustica united with Acustica*, Vol. 105, No. 1, 2019. https://doi.org/10.3813/AAA.919292.

[17] Teruna, C., Avallone, F., Casalino, D., and Ragni, D., "Numerical investigation of leading edge noise reduction on a rod-airfoil configuration using porous materials and serrations," *Journal of Sound and Vibration*, Vol. 494, 2021. https://doi.org/10.1016/j.jsv.2020.115880.

[18] Rego, L., Ragni, D., Avallone, F., Casalino, D., Zamponi, R., and Schram, C., "Jet-installation noise reduction with flow-permeable materials," *Journal of Sound and Vibration*, Vol. 498, 2021, p. 115959. https://doi.org/10.1016/j.jsv.2021.115959.

[19] Rego, L., Avallone, F., Ragni, D., and Casalino, D., "On the mechanisms of jet-installation noise reduction with flow-permeable trailing edges," *Journal of Sound and Vibration*, Vol. 520, 2022. https://doi.org/10.1016/j.jsv.2021.116582.

[20] Mengle, V. G., Brusniak, L., Elkoby, R., and Thomas, R. H., "Reducing Propulsion Airframe Aeroacoustic Interactions with Uniquely Tailored Chevrons: 3. Jet-Flap Interaction," *12th AIAA/CEAS Aeroacoustics Conference*, Cambridge, MA, USA, 2006. https://doi.org/10.2514/6.2006-2435.

[21] Slooff, J. W., de Wolf, W. B., van der Wal, H. M. M., and Maseland, J. E. J., "Aerodynamic and aero-acoustic effects of flap tip fences," Tech. rep., Dutch National Aerospace Laboratory - NLR, NLR-TP-2002-004, 2002.

[22] Rubio Carpio, A., Avallone, F., Ragni, D., Snellen, M., and van der Zwaag, S., "Quantitative criteria to design optimal permeable trailing edges for noise abatement," *Journal of Sound and Vibration*, Vol. 485, 2020. https://doi.org/10.1016/j.jsv.2020.115596.

[23] Luesutthiviboon, S., Malgoezar, A., Snellen, M., Sijtsma, P., and Simons, D., "Improving source discrimination performance by using an optimized acoustic array and adaptive high-resolution CLEAN-SC beamforming," *7th Berlin Beamforming Conference*, Berlin, Germany, 2018.

[24] Luesutthiviboon, S., Malgoezar, A. M., Merino-Martinez, R., Snellen, M., Sijtsma, P., and Simons, D. G., "Enhanced HR-CLEAN-SC for resolving multiple closely spaced sound sources," *International Journal of Aeroacoustics*, Vol. 18, No. 4-5, 2019, pp. 392–413. https://doi.org/10.1177/1475472X19852938.

[25] Mueller, T. J., *Aeroacoustic Measurements*, 1st ed., Springer-Verlag, Berlin, Germany, 2002. https://doi.org/10.1007/978-3-662-05058-3.

[26] Brooks, T. F., and Humphreys, W. M., "Effect of directional array size on the measurement of airframe noise components," *5th AIAA/CEAS Aeroacoustics Conference and Exhibit*, American Institute of Aeronautics and Astronautics Inc, AIAA, Bellevue, WA, USA, 1999. https://doi.org/10.2514/6.1999-1958.

[27] Sijtsma, P., "Phased array beamforming applied to wind tunnel and fly-over tests," Tech. rep., National Aerospace Laboratory (NLR), Amsterdam, The Netherlands, 2010. URL www.nlr.nl.